Original Article

JCBFM

Journal of Cerebral Blood Flow & Metabolism
2020, Vol. 40(10) 2098–2114

DOI: 10.1177/0271678X19886240
journals.sagepub.com/home/jcbfm
SAGE

High spatiotemporal vessel-specific hemodynamic mapping with multi-echo single-vessel fMRI

Yi He[1,2,3], Maosen Wang[1,2] and Xin Yu[1,4]

Abstract

High-resolution fMRI enables noninvasive mapping of the hemodynamic responses from individual penetrating vessels in animal brains. Here, a 2D multi-echo single-vessel fMRI (MESV-fMRI) method has been developed to map the fMRI signal from arterioles and venules with a 100 ms sampling rate at multiple echo times (TE, 3–30 ms) and short acquisition windows (<1 ms). The T_2*-weighted signal shows the increased extravascular effect on venule voxels as a function of TE. In contrast, the arteriole voxels show an increased fMRI signal with earlier onset than venules voxels at the short TE (3 ms) with increased blood inflow and volume effects. MESV-fMRI enables vessel-specific T2* mapping and presents T2*-based fMRI time courses with higher contrast-to-noise ratios (CNRs) than the T2*-weighted fMRI signal at a given TE. The vessel-specific T2* mapping also allows semi-quantitative estimation of the oxygen saturation levels (Y) and their changes (ΔY) at a given blood volume fraction upon neuronal activation. The MESV-fMRI method enables vessel-specific T2* measurements with high spatiotemporal resolution for better modeling of the fMRI signal based on the hemodynamic parameters.

Keywords

Hemodynamic signal, multi-echo fMRI, neurovascular coupling, single-vessel fMRI, vascular dynamics

Received: 28 April 2019; Revised 20 September 2019; Accepted: 7 October 2019

Introduction

Functional MRI (fMRI) has been developed to noninvasively map the large-scale brain function.[1–9] With high field MRI, numerous efforts have been made to improve the spatial specificity for functional brain mapping.[10–13] The increased signal-to-noise ratio (SNR) inherent to high field MRI enables detection of functional cortical columns[14–20] and laminar-specific fMRI signals in both animal and human brains.[21–30] Given the vascular hemodynamic origin of the fMRI signal,[31,32] when the spatial resolution of fMRI is improved to distinguish individual penetrating vessels in the cortex, the fMRI signal can be mapped from individual vessel voxels in both rat and cat brains.[22,26,33] In particular, penetrating venules dominate the BOLD signal, and penetrating arterioles mainly highlight the iron oxide particle-based cerebral blood volume (CBV) signal from the two-dimensional (2D) T2*-weighted images.[33,34] Instead of the echo-planar imaging (EPI)-fMRI method, the fast low-angle shot (FLASH) method with reshuffled line-scanning fMRI,[23,35] or the balanced steady-state free precession (bSSFP) method[36,37] has been implemented to map the single-vessel fMRI in both task-related or resting-state conditions.[33]

Optical methods have been routinely used to characterize the hemodynamic microvascular origin of the

[1]Translational Neuroimaging and Neural Control Group, High Field Magnetic Resonance Department, Max Planck Institute for Biological Cybernetics, Tuebingen, Germany
[2]Graduate Training Centre of Neuroscience, International Max Planck Research School, University of Tuebingen, Tuebingen, Germany
[3]Danish Research Centre for Magnetic Resonance, Centre for Functional and Diagnostic Imaging and Research, Copenhagen University Hospital Hvidovre, Hvidovre, Denmark
[4]Athinoula A. Martinos Center for Biomedical Imaging, Massachusetts General Hospital and Harvard Medical School, Charlestown, MA, USA

Corresponding author:
Xin Yu, Max-Planck-Ring 11, Tuebingen 72076, Germany.
Email: xyu9@mgh.harvard.edu

fMRI signal in animal brains.[38–42] By measuring the absorption spectrum of oxy- and deoxy-hemoglobin, the blood oxygen saturation changes in cortical vessels can be estimated upon neural activation.[43–46] Using two-photon microscopic (2-PM) imaging, the laminar and temporal features of neural activity-coupled arteriole dilation or pericyte-controlled capillary dilation, as a direct measurement of vascular volume change upon neuronal activation, and the blood flow changes can be integrated to interpret the fMRI signal.[38–40,47,48] Gagnon et al.[42] have implemented the vessel-specific oxygen saturation measurement based on the pO2-nanosensor in the reconstructed 3D cerebrovasculature model of rodent brains, showing a step forward in estimating the BOLD signal from previous fMRI modeling studies.[49–53] In particular, the altered arteriole oxygen saturation levels in the cerebrovasculature have demonstrated the direct arteriole contribution to the BOLD signal.[42] This study is an extension of the pial vessel oxygen tension measurement with the oxygen sensor, showing that the oxygen saturation level can be less than 80% in an artery with a diameter of less than 50 μm.[54] Simultaneous optical measurements of the hemodynamic responses with fMRI have revealed a strong temporal correlation,[40,55] but the conventional fMRI method does not provide a vessel-specific validation platform to distinguish the fMRI signal from arteriole and venule voxels. Due to the limited spatiotemporal resolution of conventional fMRI methods, the vessel-specific fMRI signal has been seldom measured to validate the modeling of the fMRI signal based on the estimated hemodynamic factors, e.g. the oxygen saturation level (Y) and the blood volume fraction (V_f).[32] The single-vessel fMRI mapping scheme enables semi-quantitative estimation of the hemodynamic parameters for modeling the vessel-specific fMRI signal directly.

In the present study, we implemented a multi-echo acquisition scheme for the line-scanning fMRI method[23,34] to measure the fMRI signal from individual vessels.[23,34] With the improved method, each k-space line was acquired consecutively along the block design paradigm, and the on/off stimulation trials were repeated for the number of phase-encoding steps.[34,35] Since only one k-space line was acquired per echo, the acquisition window could be significantly reduced to ~1 ms, which is much shorter than the readout echo train (10–20 ms) of the EPI method. The short acquisition window not only avoided the long echo train-induced extra T_2*-weighting under the high magnetic field but also shortened the minimal TE.[22,56–60] Here, we used the multi-echo single-vessel fMRI (MESV-fMRI) method to measure the MRI signal at different TEs and hence specify the spatiotemporal patterns of the T_2* signal changes from distinct arteriole and venule voxels. This work also enables direct estimation of the dynamic changes of the oxygenation saturation level from individual vessel voxels at a given vessel volume fraction.

Materials and methods

Animal preparation

All animal experiments were performed according to a protocol approved by the animal protection committee (KY 02/14, Regierungspräsidium Tuebingen, Germany), and in accordance with the guidelines of the European Communities Council Directive 2010/63/EU. Experiments were reported according to the Animal Research: Reporting in Vivo Experiments (ARRIVE) guidelines.

fMRI experiments were performed on five male Sprague Dawley rats. All procedures have been described in a previous study.[33,34,61,62] Rats were initially anesthetized with isoflurane (5% induction, 1.5% maintenance), and orally intubated and placed on a mechanical ventilator (SAR-830/AP, CWE Inc.). Plastic catheters were inserted into the right femoral artery and vein to allow monitoring of arterial blood gasses and administration of anesthetics. After surgery, each rat was given an intravenous bolus of α-chloralose (80 mg/kg), and isoflurane was discontinued. Anesthesia was maintained with a constant infusion of α-chloralose (26.5 mg/kg/h). The animals were placed on a heated pad to maintain a rectal temperature at 37°C while in the magnet. Each animal was secured in a head holder with a tooth-bar to prevent head motion. End-tidal CO_2, rectal temperature, tidal pressure of ventilation, heart rate, and arterial blood pressure were continuously monitored during the experiment. Arterial blood gas levels were checked periodically, and corrections were made by adjusting the respiratory volume or administering sodium bicarbonate to maintain blood gas levels when required. An intravenous injection of pancuronium bromide (4.0 ± 0.18 mg/kg, mean ± SD, $n = 5$ rats) was given once per hour to reduce motion artifacts. Voluntary respiration-induced resonance offset reduced significantly following the administration of the pancuronium injection.

MRI image acquisition

All images were acquired with a 14.1 T/26 cm horizontal bore magnet (Magnex), interfaced to an AVANCE III console (Bruker, Germany) and equipped with a 12 cm gradient set, capable of providing 100 G/cm with a rise time of 150 μs (Resonance Research).

A transceiver surface coil with a 6 mm diameter was used to acquire images.

MESV-fMRI. Previously, the line-scanning method was applied to acquire a single k-space line along the on/off block design to map the fMRI signal with high spatial and temporal resolution.[23,34,35] Here, multi-gradient echoes were implemented in the single-vessel line-scanning fMRI method. In contrast to the multi-echo EPI-fMRI and FLASH-fMRI methods,[63–66] MESV-fMRI acquired only one k-space line for each echo at every time-of-repetition (TR) during an on/off stimulation block-design trial, and the k-space was filled sequentially by repeating the fMRI block-design stimulation trials for the number of phase-encoding steps (Figure 1(b)). This acquisition scheme sampled fMRI signals from multiple echoes ranging from 3 ms to 30 ms at every 100 ms with an acquisition window for each echo of less than 1–2 ms.

A 2D multiple gradient echo (MGE) sequence was modified to perform multi-echo line-scanning fMRI with the following parameters: TEs, 3 ms, 6.5 ms, 10 ms, 13.5 ms, 17 ms, 20.5 ms, 24 ms, 27.5 ms, 31 ms; TR, 100 ms; flip angle, 22°; matrix, 96×64; slice thickness, 400 μm; in-plane resolution, 100×100 μm; acquisition bandwidth, 96 kHz. Two saturation slices were applied every TR to suppress the signal outside of the field of view (FOV) and hence reduce the potential aliasing effect along the phase-encoding direction. The frequency-encoding direction was set along the z0 direction toward the lung to reduce the respiration-induced resonance offset. The block-design stimulation paradigm was used in the MESV-fMRI experiment. The electrical stimulation was delivered by a stimulation isolator (AD Instruments) (2.0 mA, 300 μs pulses repeated at 3 Hz) through two needle electrodes that were inserted between digits of the forepaw. The block-design paradigm consisted of 60 dummy scans to reach steady state, followed by 10 pre-stimulation scans, 20 scans during electrical stimulation, and 100 post-stimulation scans (with a total of 13 s for each on/off stimulation experiment). For image acquisition, only one single-phase k-space line was acquired at each TE per 100 ms before the second set of k-spaces was filled during the block design trial (Supplementary Fig. 1). Each trial consisted of three epochs of on/off stimulation periods with a total of 390 TRs. The trials were repeated for the number of phase-encoding steps. The total duration was 40 min, and –three to six MESV-fMRI trials were acquired for each rat.

The single-vessel arteriole-venule map. A 2D MGE sequence was used to detect individual arterioles and venules with the following parameters: TR, 50 ms; TEs, 2.5 ms, 5 ms, 7.5 ms, 10 ms, 12.5 ms, 15 ms, 17.5 ms; flip angle, 40°; matrix, 192×128; in-plane resolution, $50\,\mu m \times 50\,\mu m$; slice thickness, 400 μm, acquisition bandwidth, 96 kHz. This slice orientation was perpendicular to the penetrating vessels and covered forepaw S1 areas based on the Paxinos atlas. The horizontal slice angle was set at 15°, and the center of the slice was positioned 1.2 mm from the cortical surface to cover layer 5 (Figure 1(a)). Similar to the previous study,[34] by averaging the MGE images acquired from the second echo to the fourth echo, the single-vessel A-V map showed the venule voxels as dark dots due to fast T_2* de-phasing, while arteriole voxels remained as bright dots due to the in-flow effect. The individual vessel voxels were determined based on their signal intensity as either higher than the mean signal intensity plus three times the standard deviation (arterioles) or lower than the mean signal intensity minus three times the standard deviation (venules) of the local areas in a 7×7 kernel. The venule voxels were color-coded in blue, and the arterial voxels were color-coded in red (Figure 1(a)). After the vessel voxels were characterized, an "imdilate" function[67,68] was applied to dilate each vessel voxel. The differences between the vessel voxels and the dilated vessel voxels specify the peri-vessel area surrounding the vessel voxels. To avoid peri-vessel voxels being overlapped by different vessel voxels, a dilating factor of 2 was chosen to set the expanded peri-vessel voxels to a width of two voxels (Figure 2(c)).

Image processing and statistical analysis

MESV-fMRI data analysis was performed using the "Analysis of Functional NeuroImages" (AFNI)[69] software (NIH) and MATLAB. A detailed description of the processing was provided in a previous study.[23]

MESV-fMRI preprocessing

The MESV-fMRI 2D k-space data were first reordered by a MATLAB script, and then reconstructed to MESV-fMRI images using a function embedded in the Bruker ParaVision 5.1 software. For AFNI analysis, a 2D registration function was applied to align all MESV-fMRI images to a template for multiple datasets acquired in the same orientation setup. To register the MESV-fMRI images with the single-vessel map, a tag-based registration method was applied. Ten to 12 tags were chosen from the venule voxels distributed around the 2D slices of the MESV-fMRI and single-vessel images. The baseline level of the MESV-fMRI images was scaled to 100, and multiple trials of block-design time courses were averaged for statistical

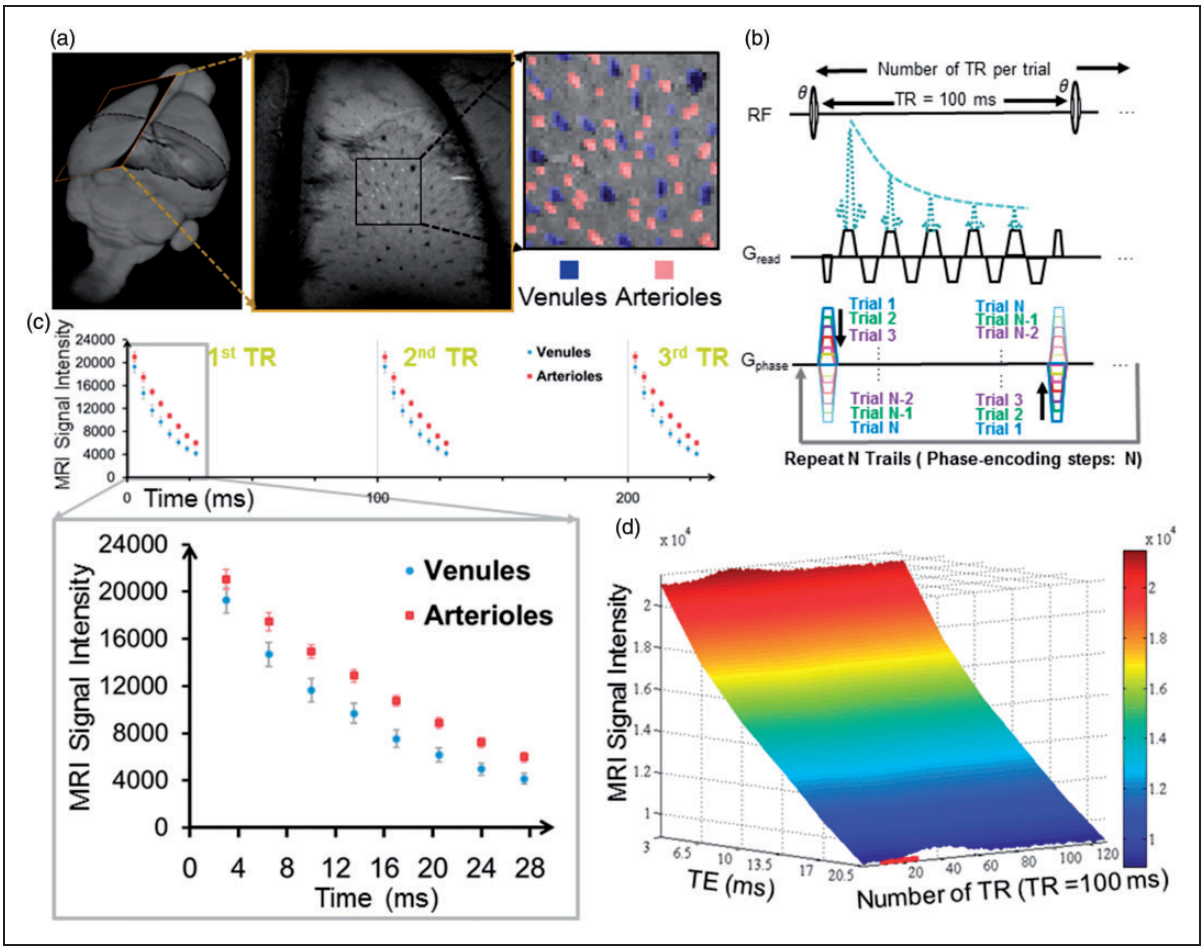

Figure 1. Mapping the vessel-specific fMRI signal with the MESV-fMRI method. (a) The 2D slice position of the A-V map was shown in the 3D rat brain (left panel). The arteriole voxels were marked as red ROIs and the venule voxels as blue ROIs (right panel), (b) MESV-fMRI pulse sequence diagram. Only one phase-encoding step was employed in each trial. The trials were repeated for the number of phase-encoding steps to fill up the k-space, (c) The signal intensity of venule voxels (blue circles) and arteriole voxels (red squares) was shown at different TEs from three consecutive TRs (100 ms). The enlarged data showed that the venule voxels had faster decay curves than the arteriole voxels (one representative rat from five rats, venules: $n = 25$, arteriole: $n = 32$, mean (95% CI)), (d) The three-dimensional plot of the mean signal intensity with multiple echoes TEs (3.5 ms to 21.5 ms) from venule voxels as a function of the on/off block design time (1 s off, 2 s on, and 10 s off).

analysis. The hemodynamic response function (HRF) was estimated by the linear regression using a tent basis function as previously reported.[34]

T_2 mapping.* T_2* values were calculated on a voxel-by-voxel basis by fitting the following exponential decay equation

$$f(t) = S_0 \times \exp(-t/T_2^*) \quad (1)$$

where t is the time variable, and S_0 is the initial signal intensity, the T_2*-based fMRI signal was estimated based on the percentage change of the T_2* value from the baseline level scaled to 100.

Contrast-to-noise ratio. Contrast-to-noise ratio (CNR)[70] was estimated based on the following equation

$$CNR = (S_P - S_B)/\sigma_B \quad (2)$$

where S_P is the peak amplitude, S_B is the mean of the baseline signal, and σ_B is the standard deviation of the baseline signal, respectively. The CNR of the fMRI signal at different echoes and the T_2*-based fMRI signal were analyzed with one-way ANOVA followed by Tukey's multiple comparison tests.

Estimation of the temporal hemodynamic features of vessel-specific fMRI signal. A two-gamma-variate fitting process was used to fit the fMRI signal acquired from

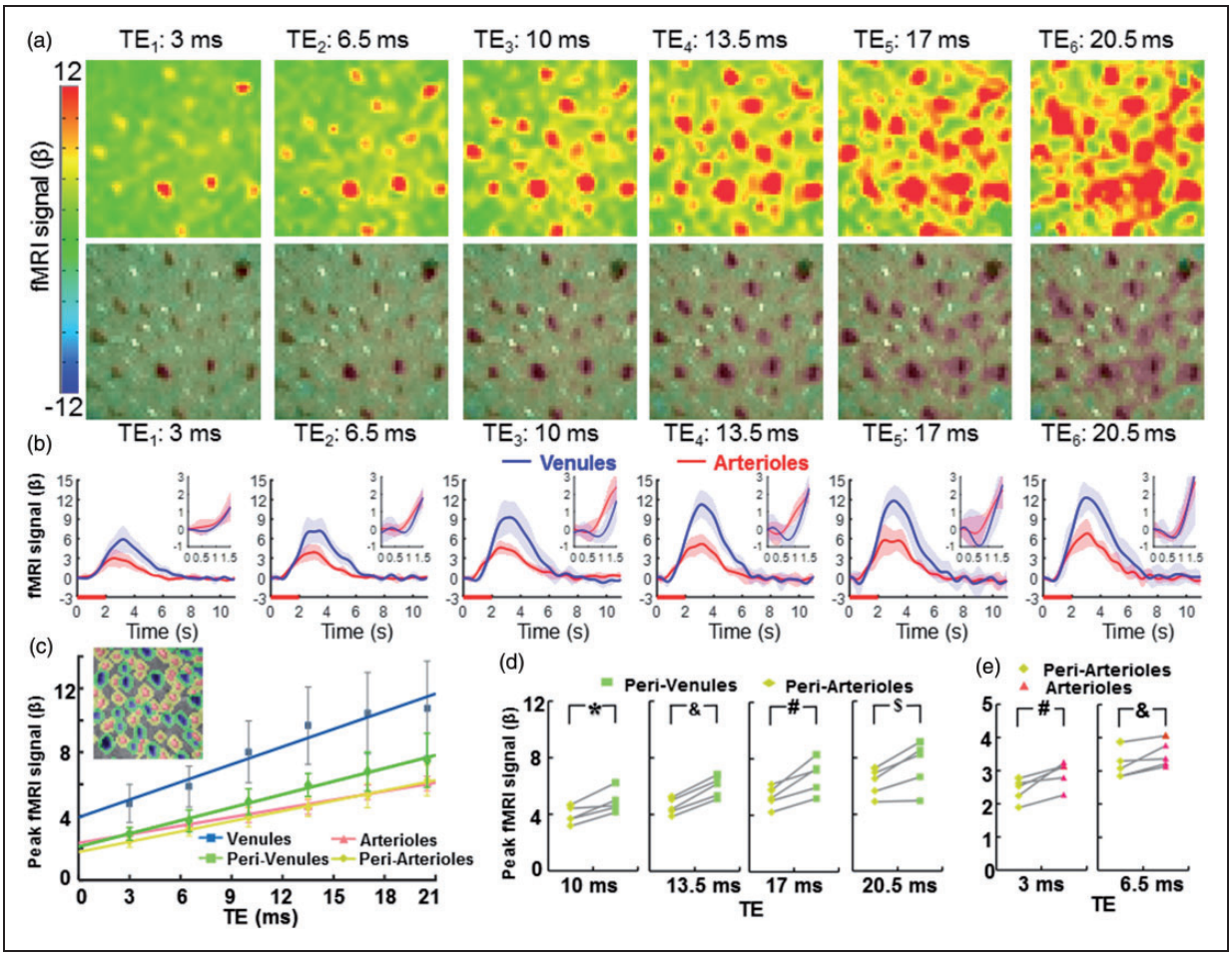

Figure 2. The vessel-specific fMRI patterns acquired at different TEs. (a) The color-coded fMRI maps were shown at six different TEs (top). The images overlapped with the A-V map represented the venule-dominated peak fMRI signal distribution patterns (bottom), (b) The averaged time courses of the fMRI signal from venule (blue) and arteriole (red) voxels ($n = 5$ rats, mean ± SD; inset: the time course from 0 s to 1.5 s after stimulus onset), (c) The peak amplitudes of the normalized fMRI signal from arteriole (red), venule (blue), peri-venule (green), and peri-arteriole (yellow) voxels were shown at different TEs ($n = 5$ rats, mean ± SD). The peak fMRI signal (β) was calculated by normalizing the baseline of the raw fMRI time course to 100. (inset: a demo A-V map with different vascular component ROIs in different colors), (d) The peak fMRI signal of peri-venule voxels was significantly higher than that of peri-arteriole voxels acquired at TEs ranging from 10 ms to 20.5 ms ($n = 5$, $^{*}p = 0.007$, $^{\&}p = 0.0001$, $^{\#}p = 0.005$, $^{\$}p = 0.012$, paired t-test), (e) The peak fMRI signal of arteriole voxels was significantly higher than that of peri-arteriole voxels acquired at TEs 3 ms and 6.5 ms ($^{\#}p = 0.012$; $^{\&}p = 0.017$, paired t-test, $n = 5$).

individual vessel voxels[71]

$$F(t) = a \times \left(t/(p \times q)\right)^{p} \times e^{p-t/q} - b \times \left(t/(r \times s)\right)^{r} \times e^{r-t/s} \quad (3)$$

where t is the temporal variable and a, p, q, b, r and s are the coefficients of the two-gamma-variate-function. The onset time (T0) was measured as an intercept with the baseline by fitting a line to the rising slope between 20% and 80% of the peak amplitude estimated from the two-gamma-variate-function.[40] The time-to-peak (TTP) and the full-width-of-half-maximum (FWHM) were estimated directly from the two-gamma-variate-function (Supplementary Figure 2).

Blood volume fraction (V_f).

$$V_f = \pi \cdot (D/2)^2/(N_{ROI} \cdot S_{voxel}) \quad (4)$$

where D is the diameter of the vessels, N_{ROI} is the mean number of voxels defining the venules and arterioles, and S_{voxel} is the area per voxel which is equal to 50 μm × 50 μm.

Estimated saturation (Y) and saturation changes (ΔY) of individual vessels[72].

$$R2* = R2 + R2' \quad (5)$$

$$R2' \ (s^{-1}) = \mathrm{V}_f \cdot \gamma \cdot 4/3 \cdot \pi \cdot \Delta\chi \cdot (1 - Y) \cdot B_0 \quad (6)$$

$$\Delta \mathrm{R2}' \quad = \gamma \cdot 4/3 \cdot \pi \cdot \Delta\chi \cdot (1 - Y) \cdot B_0 \cdot \Delta V_f - V_f \cdot \gamma \cdot 4/3 \cdot \pi \cdot \Delta\chi \cdot B_0 \cdot \Delta Y \quad (7)$$

where $R2$ is the relaxation rate of vessels, and $R2'$ is a contribution to the signal relaxation rate from local field inhomogeneities. Here $R2$ was estimated by the $R2$ fitting of gray matter from Pohmann et al.'s[73] work which provided the following equation fitted by using different field strengths (4.0 T, 9.4 T, 11.7 T, and 16.4 T): $\mathrm{R2} = 1/(\mathrm{a} \cdot \mathrm{e}^{-\frac{B_0}{b}}) = 1/(89.6 \cdot \mathrm{e}^{-\frac{14.1}{12.59}}) = 34.2 \ \mathrm{s}^{-1}$.

In equations (6)[72] and (7),[72] V_f is the blood volume fraction, γ is the nuclear gyromagnetic ratio, $\Delta\chi$ is the susceptibility difference between deoxygenated and oxygenated blood with the hematocrit level of 0.4,[74,75] Y is the oxygen saturation of vessels, B_0 is the main static magnetic field, and ΔY is the saturation changes of individual vessels.

Substituting $\gamma = (2.675 \cdot 10^4 \ \mathrm{rad/s})/\mathrm{Gauss}$, $\Delta\chi = 0.8 \cdot 10^{-7}$ and $\mathrm{B}_0 = 14.1$ Tesla into the equations gives:

$$R2' \ (s^{-1}) = 1263.36 \cdot V_f \cdot (1 - Y) \quad (8)$$

$$\Delta \mathrm{R2}' = 1263.36 \cdot (1 - Y) \cdot \Delta V_f - 1263.36 \cdot V_f \cdot \Delta Y \quad (9)$$

According to equations (4) to (9), the saturation Y and saturation changes ΔY were calculated based on the measured $R2^*$ and estimated $R2$ from vessel voxels. A paired Student's t-test was performed to compare the mean signal intensity, T0, TTP, and the FWHM of the T_2^* fMRI signal from the venule voxels and arteriole voxels. The error bar in each graph represents the standard deviation (SD) of the mean or 95% confidence interval (CI).

Results

Mapping the T_2^*-weighted fMRI signal from arterioles and venules with MESV-fMRI

Individual arterioles and venules penetrating the cortex could be directly mapped by an inflow-based MGE sequence,[34] which has been previously proposed for the human brain mapping to identify pial arteries and veins.[66] At shorter TEs, both arterioles and venules were detected as brighter voxels due to the inflow effect. In contrast, at longer TEs, only venules were detected as darker voxels due to the fast T_2^* decay of the deoxygenated venule blood, but arterioles were not differentiated because of the similar susceptibility of oxygenated blood to the surrounding parenchyma voxels. MGE images at different TEs were integrated into the A-V map, demonstrating arterioles as bright dots and venules as dark dots (Figure 1(a)). The size of the penetrating vessels detected by the A-V map ranged from 30 to 70 μm in the rat brain.[34] The vessel diameter was previously estimated based on the vessel distance of the A-V map in comparison to the mean distance of penetrating vessels in the 3D reconstruction of the vascular network characterized by 2-PM imaging.[42,76,77]

The same slice orientation was applied to both the MESV-fMRI images and the A-V map so that the vessel-specific fMRI signal could be identified from individual arteriole and venule voxels penetrating the deep layer cortex. The primary somatosensory (S1) cortex was covered in the A-V map (Figure 1(a)). The fMRI signal detected by the MESV-fMRI method was acquired from the multi-echoes in a reshuffled k-space acquisition scheme (Figure 1(b), Supplementary Figure 1). Figure 1(c) illustrates the T_2^* decay curves of arteriole and venule voxels as a function of TE, which were acquired every 100 ms based on an on/off block design paradigm. Figure 1 (d) shows the three-dimensional plot of the mean signal intensity acquired at multiple echoes from venule voxels as a function of time, demonstrating the increased T_2^*-weighted signal at different TEs of the decay curves upon stimulation.

The detailed functional patterns were characterized at different TEs ranging from 3 ms to 20.5 ms using MESV-fMRI (Figure 2(a) and (b), Supplementary Movie 1; the normalized fMRI signal at different TEs from venule and arteriole voxels, Supplementary Figure 3). The peak fMRI signal acquired at different TEs was located primarily on venule voxels which is consistent with the previous studies.[33,34] Even at short TEs, the peak fMRI signal matched well with the venules voxels detected in the A-V map, which could be caused by the oxy/deoxy-hemoglobin changes in the venule blood, i.e. the BOLD effect, since the venule blood has a very short T_2.[56,78] The venule-dominated BOLD fMRI responses were also demonstrated by comparing the peak amplitude of fMRI time courses from arteriole and venule voxels (Figure 2(c)). The other voxels, enriched with capillaries or small vessels not identified by the A-V map, showed a higher fMRI peak amplitude than arteriole voxels, but lower than venule voxels at different TEs (Supplementary Figure 4).

The MESV-fMRI multi-echo scheme enabled specification of the extravascular effect on the functional patterns with different T_2^* weighting, as well as the potential contribution from the T_1-weighted signal due to cerebral blood flow changes from arterioles. To better characterize the fMRI signal from different vascular components, the parenchyma voxels

surrounding arterioles, i.e. peri-arteriole voxels, and parenchyma voxels surrounding venules, i.e. peri-venule voxels, were defined based on a dilatory function to label the voxels surrounding each individual vessel voxels. The peak fMRI signal from peri-arteriole and peri-venule voxels was compared with that of the arteriole and venule voxels at different TEs, showing highly proportional BOLD signal changes as a function of TE (Figure 2(c)). Linear fitting detected positive intercepts of the fMRI signal at zero echo time, which can be primarily contributed to the inflow effects as previously reported.[79] Also noteworthy is that the non-linear relationship of BOLD signal and short echo times[79] can potentially deviate the flow-related TE-independent signal changes, in particular, the intercept values of the venule voxels given the very short T2* of deoxygenated blood.[42,56,78]

Quantitative analysis demonstrated that the peak fMRI signal from peri-venule voxels was significantly higher than that from peri-arteriole voxels at longer TEs ranging from 10 to 20 ms (Figure 2(d)). In addition, the TE-dependent peak fMRI signal from the other non-vessel voxels showed a similar amplitude to that of the peri-venule voxels (Supplementary Figure 5). These results indicate that the extravascular effect from venules can be directly measured from the peri-venule voxels and the other non-vessel voxels enriched with capillaries or small vessels using the MESV-fMRI method. In contrast, the peak fMRI signal from arterioles was significantly higher than that from the peri-arteriole voxels for shorter TEs (3 and 6.5 ms), but not for longer TEs (Figure 2(e)). This result indicates that the inflow effect due to activity-coupled cerebral blood flow and volume changes directly contributes to the fMRI signal acquired at short TEs. Besides the peak fMRI signal, the fMRI signal acquired from 1 s to 2 s following stimulus onset was compared for arteriole, venule, peri-arteriole and peri-venule voxels at the short TE (3 ms) (Supplementary Figure 6). The early fMRI signal (e.g. 1 s, 1.2 s after stimulus onset) from arteriole voxels was significantly higher than that from the other voxels. These results indicate that the blood flow and volume-dependent arteriole-specific fMRI signal could be detected by MESV-fMRI independently of the BOLD effect dominating the fMRI signal in venule voxels.

Distinguishing the T_2-based fMRI signal from arterioles and venules with MESV-fMRI*

We also estimated the T2* values every 100 ms by fitting the T_2* decay curves acquired from each voxel. Figure 3(a) demonstrates the T_2* maps acquired at 2 s and 3 s after stimulus onset. The estimated T_2* values of venules voxels were much lower than the arteriole and non-vessel parenchyma voxels due to the high susceptibility of the deoxygenated venule blood. Because of the similar susceptibility of arteriole blood with a high concentration of oxy-hemoglobin to that of non-vessel parenchyma voxels enriched with capillaries or small vessels, the arteriole and non-vessel parenchyma voxels showed similar T_2* values. Figure 3(b) illustrates an example of fitting the T2* decay curves and the averaged time courses of T_2* values of arteriole and venule voxels. The transverse relaxation rate change, $\Delta R2^*$ ($1/T_2^*$), of individual venule voxels is $6.78 \pm 1.02\ s^{-1}$, while that of individual arteriole voxels is $2.60 \pm 0.18\ s^{-1}$ (mean $\pm$ 95% CI), which are comparable to the $\Delta R2^*$ ($4.15 \pm 0.44\ s^{-1}$) value measured in the superficial cortical layers with the 15.2 T scanner.[80] Also, the ratio of $\Delta R2^*/R2^*$ of venule (0.102 ± 0.013, mean $\pm$ 95% CI) and arteriole (0.056 ± 0.004, mean $\pm$ 95% CI) voxels is similar to the previously reported value of $\sim$0.053 (calculated from $\Delta R2^*/(1000/T2^*) = 3.09/(1000/17.1\ ms)$) from the rat somatosensory cortex measured at 15.2 T.[80]

Similar to previous multi-echo EPI studies,[63,81,82] the CNR of the T_2*-based fMRI signal changes was significantly higher than that of the T_2*-weighted fMRI signal changes acquired at each echo for both arteriole and venule voxels (Figure 3(d) and (e)). In addition, the T_2*-based fMRI signal showed a similar or higher CNR than that of the averaged T_2*-weighted image acquired at all TEs (Figure 3(d) and (e)). The higher CNR of the T2*-based fMRI signal allows better characterization of the temporal hemodynamic features of individual vessels. Similar to the T_2*-weighted functional maps acquired at different TEs (Figure 2), the peak T_2*-based fMRI signal was primarily located at the penetrating venules (Figure 4(b), Supplementary Movie 2). The vessel-specific temporal features of the T_2*-based fMRI signal could be characterized from individual arterioles and venules. Figure 4(c) shows the time courses of the T_2*-based fMRI signal with fitting curves acquired from individual arteriole and venule voxels. The averaged time courses of the T_2*-based fMRI signal showed an earlier onset from arteriole voxels than from venule voxels (Figure 4(d)). The T_2* value of arteriole voxels detected at 0.8 s after stimulus onset was significantly higher than that of venule voxels, which was reversed at later time points, e.g. at 1.8 s after stimulus onset (Figure 4(e) and (f)). This is consistent with a previous study using the EPI-fMRI method to decipher the distinct vascular components contributing to the BOLD-fMRI signal.[22] The onset time (T0), time-to-peak (TTP) and full-width-of-half-maximum (FWHM) plots of the T_2*-based fMRI signal readily separated

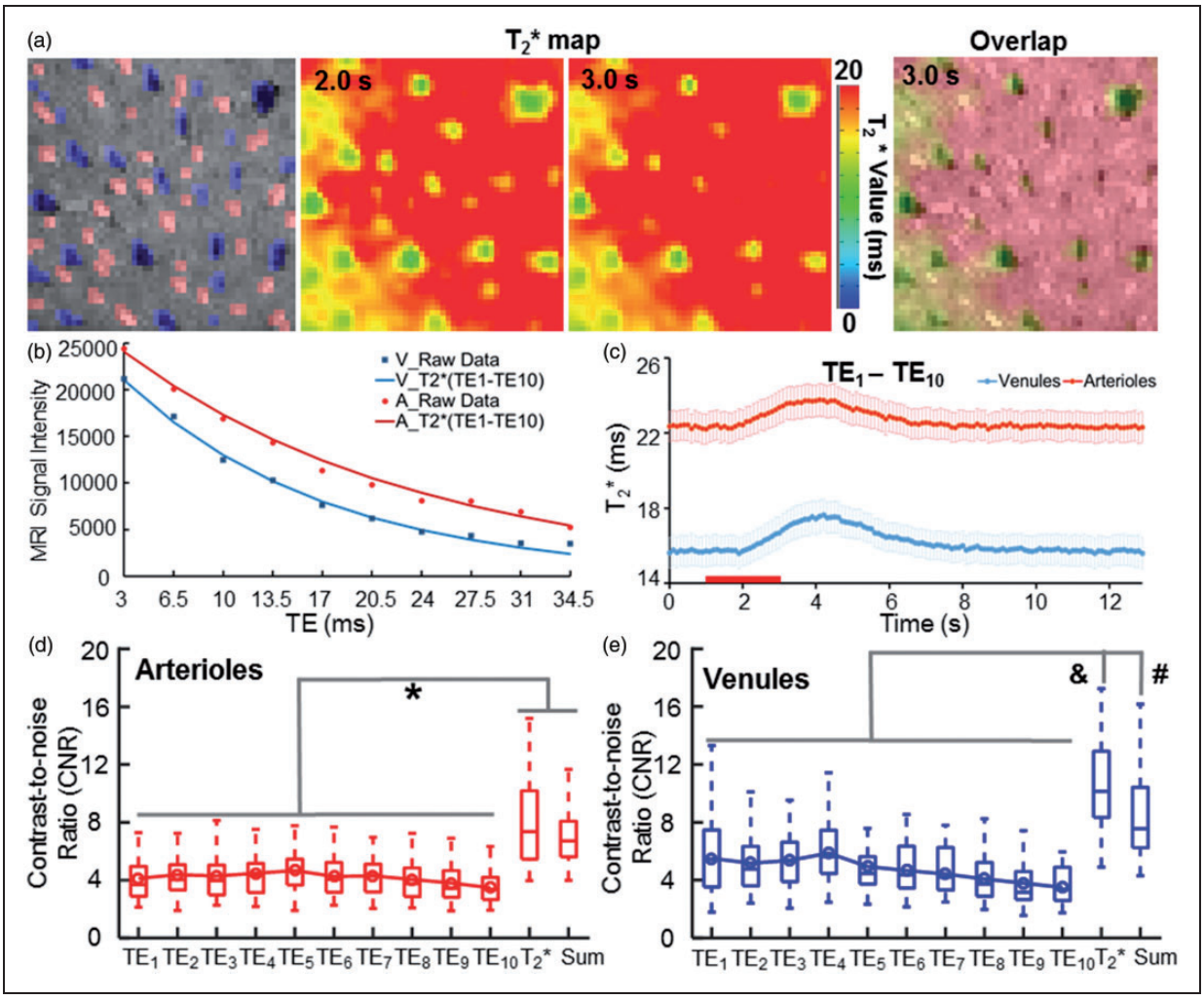

Figure 3. The vessel-specific T_2* map with the MESV-fMRI method. (a) The individual arterioles (red) and venules (blue) voxels were identified in the A-V map. The T_2* maps of the 2D slice acquired at 2 s and 3 s after stimulus onset (left and middle panels). The T_2* map (3 s) overlapped with the A-V map showed all venule voxels with a shorter T_2* time than the other voxels (right panel), (b) The T_2* decay signal from a representative venule was fitted with decay curves with 10 TEs. (c) The T_2* values were plotted as a function of time during the on/off block-design from venule and arteriole ROIs ($n = 5$ rats, mean (95% CI)), (d–e) The contrast-to-noise ratios (CNRs) of the T_2*-weight fMRI signal acquired at different TEs were significantly lower than the CNR of the T_2*-based fMRI signal from both arteriole and venule voxels. The T_2*-based fMRI signal showed a similar or higher CNR than the CNR of the averaged T_2*-weighted image of all TEs. ($^{*}F = 31.4$, $p < 0.00001$, $^{\&}F = 28.12$, $p < 0.00001$, $^{\#}F = 28.12$, $p < 0.01$, one-way ANOVA followed by Tukey's multiple comparison test).

arteriole and venule responses into distinct clusters (Figure 4(g)). The T0 and TTP of the arteriole voxels were significantly shorter than those of the venule voxels (Figure 4(h)), demonstrating the potential hemodynamic signal propagation through the cerebrovasculature directly mapped by MESV-fMRI, which has not been well detected by the T2*-weighted single-vessel fMRI method.[33,34] Therefore, MESV-fMRI enables characterization of the temporal hemodynamic features of the fMRI signal detected from individual arteriole and venules.

Estimating the baseline oxygen saturation level (Y) and its changes (ΔY) from individual vessels

The MESV-fMRI method allows estimation of the T2* signal from arterioles or venule voxels (though the flow and volume changes detected at the short TE may deviate the T2* fitting), providing the simplified "vessel voxel" condition for the analytical modeling of the NMR dephasing behavior in the brain tissue as proposed by Yablonskiy and Haacke.[72] Assuming the static dephasing regime, we provide a semi-quantitative

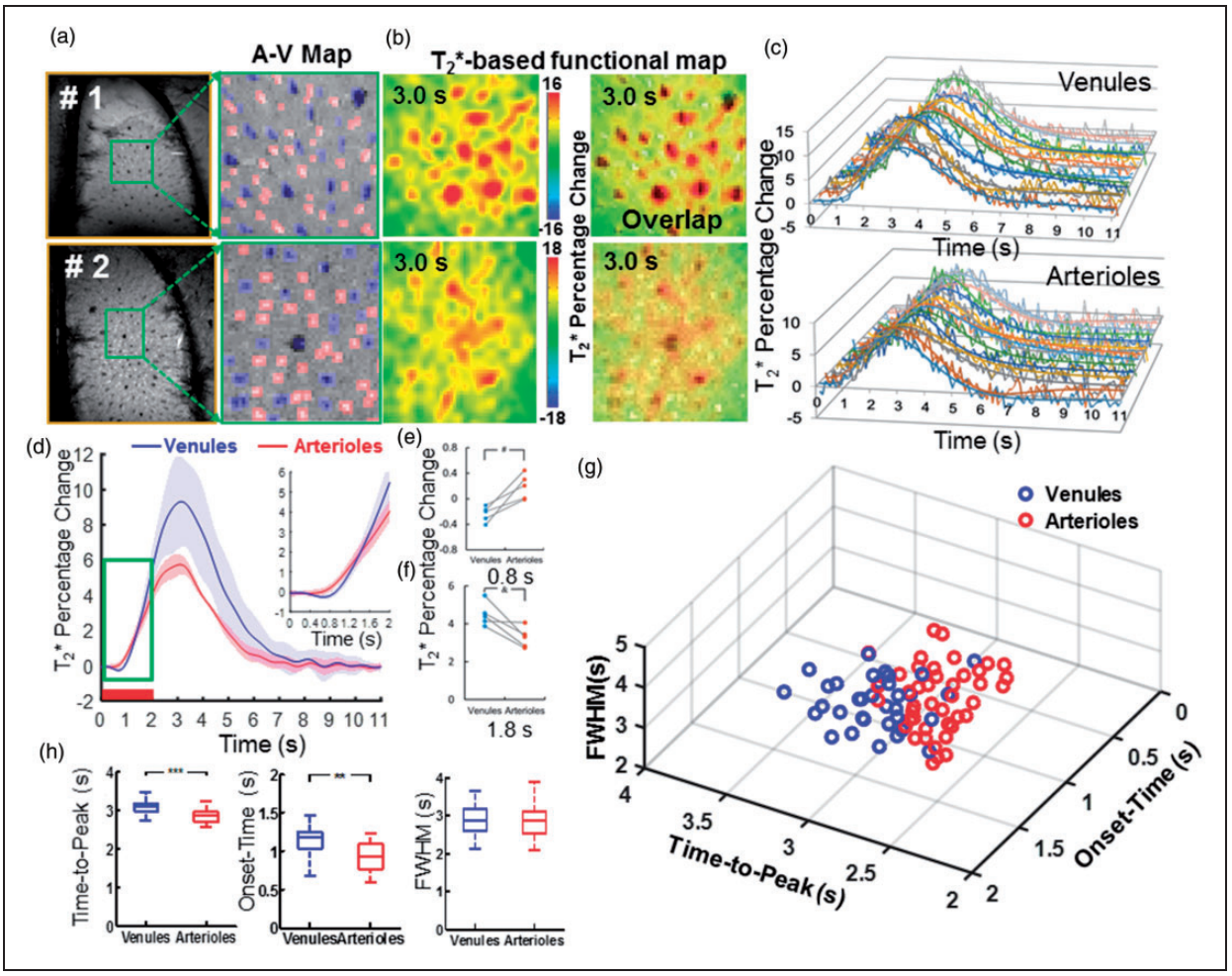

Figure 4. The hemodynamic feature of the T_2*-based fMRI signal with the MESV-fMRI method. (a) The A-V maps from two representative rats of five rats showed arteriole (red) and venule (blue) ROIs, (b) The T_2*-based fMRI maps were represented at 3.0 s after stimulus onset (the left panel), and the fMRI maps were overlapped with A-V maps, (c) The time courses (raw data and fitting curves) of the T_2*-based fMRI signal were plotted from the individual venule voxels (upper panel) and arteriole voxels (lower panel) of one representative rat, (d) The averaged time courses of the T_2* fMRI signal from venule (blue) and arteriole (red) voxels ($n = 5$ rats, mean ± SD; inset: the time course from 0 s to 2.0 s after stimulus onset), (e–f) T_2* fMRI signal percentage changes from arteriole and venule voxels were shown at 0.8 s and 1.8 s after stimulation onset from individual rats ($^{\#}p = 0.006$; $^{\&}p = 0.012$, paired t-test, $n = 5$), (g) The 3D plot of onset-time (T0), time-to-peak (TTP), and the full-width-of-half-maximum (FWHM) of the T_2* fMRI signal from individual arteriole (red circles, 43, $r^2 > 0.7$) and venule (blue circles, 34, $r^2 > 0.8$) voxels demonstrated two distinct clusters, (h) The quantitative analysis of the TTP, T0, and FWHM of the T_2* fMRI signal from venule (blue) and arteriole (red) voxels ($^{**}p = 6.2 \times 10^{-8}$, $^{***}p = 8.1 \times 10^{-9}$, unpaired t-test, arteriole voxels, 43, venule voxels, 34).

estimation of the hemodynamic factor, oxygen saturation level (Y) from individual vessel voxels based on the measured R2* value (converted to R2′ based on the previously measured R2 using the same system[73]) and blood volume fraction (V_f). Figure 5 shows the vessel-specific Y maps of individual venule and arteriole voxels, assuming that the vessel diameter is either 35 µm (Figure 5(b)) or 50 µm (Figure 5(c)). Supplementary Table 1 provided the mean Y of venules (0.39–0.65 up to 50 µm) and arterioles (0.74–0.94 from 35 µm to 70 µm). In parallel, we also calculated the oxygenation saturation changes (ΔY) during stimulation based on the T2*-based fMRI signal at given arteriole V_f changes (ΔDiameter: 5%, 10%, 15%) and no venule V_f changes (ΔDiameter = 0) based on previous studies.[38,39,54] Based on the estimated baseline vessel diameter (35 µm vs. 50 µm), the vessel-specific ΔY maps of individual venule and arteriole voxels were presented at varied ΔV_f values (Figure 5(e), (f), (h) and (i)), showing the venule ΔY at 6.4–11.1% and arteriole ΔY at 3.3–6.5% with ΔV_f at 5% (Figure 5(g) and (j)). Supplementary Table 2 shows the mean ΔY of venules and arterioles with the diameter ranging from 35 µm to 70 µm, respectively.

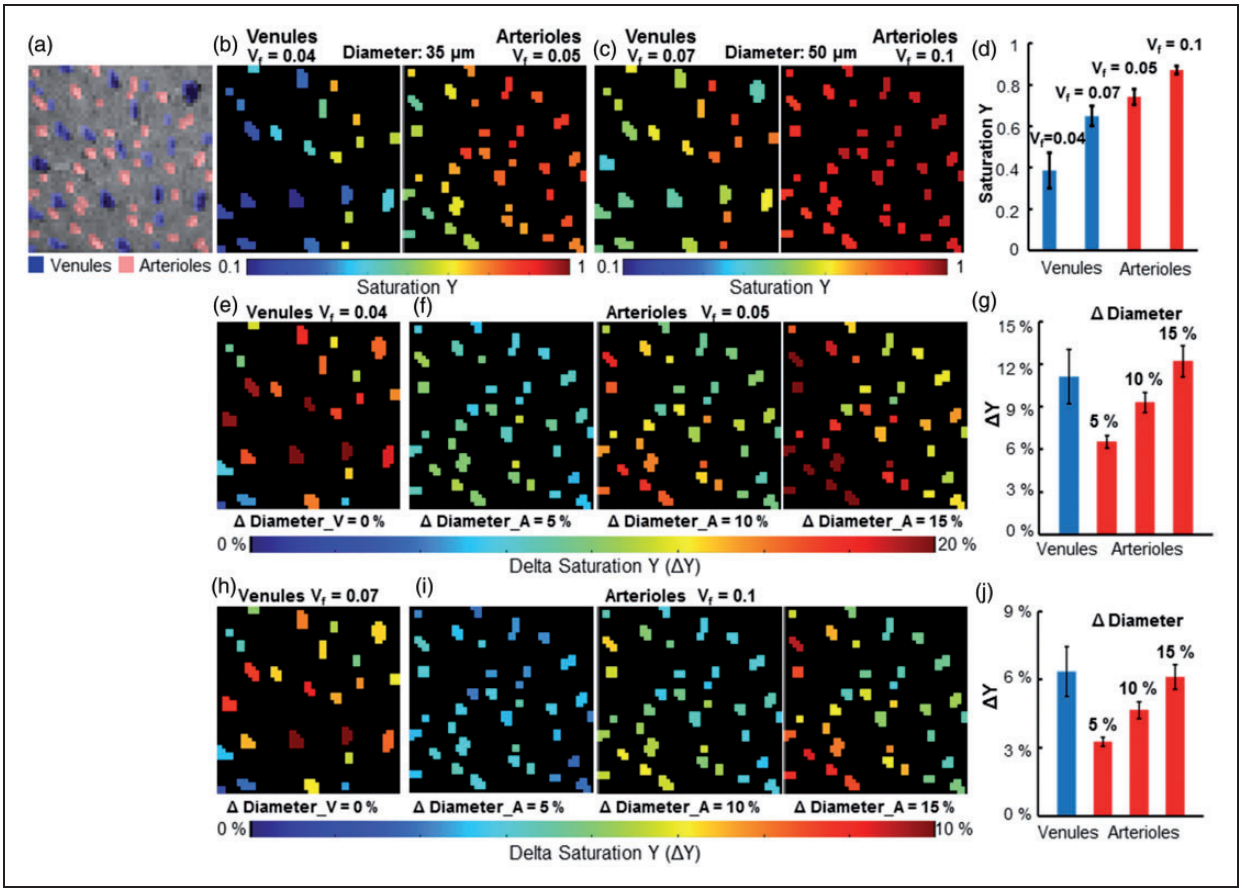

Figure 5. The estimated saturation Y maps and saturation Y changes (ΔY) maps of individual vessels. (a) The individual arterioles (red) and venules (blue) voxels were identified in the A-V map, (b) The saturation Y map of venules (the left panel, $V_f = 0.04$) and arterioles (the right panel, $V_f = 0.05$) when all venules and arterioles were assumed to have a diameter of 35 μm, (c) The saturation Y map of venules (the left panel, $V_f = 0.07$) and arterioles (the right panel, $V_f = 0.1$) when all venules and arterioles were assumed to have a diameter of 50 μm, (d) The mean Y saturation of venules and arterioles when the diameters of all vessels were assumed to be 35 μm (Y_V = 0.386 ± 0.086, Y_A = 0.741 ± 0.038, mean (95% CI)) or 50 μm (Y_V = 0.649 ± 0.049, Y_A = 0.871 ± 0.019, N_venules = 25, N_arterioles = 35, mean (95% CI)), (e) The saturation changes ΔY maps of individual venules when the diameter of venules was assumed to be 35 μm and not to increase after sensory stimulation, (f) The saturation changes ΔY maps of individual arterioles when the diameter of arterioles was assumed to be 35 μm and dilated by 5% (the left panel), 10% (the middle panel) and 15% (the right panel) after sensory stimulation, (g) The mean ΔY saturation of venules and arterioles when the diameter of vessels was assumed to be 35 μm (ΔY_V = 11.14 ± 1.91%, N_venules = 25; 5% diameter changes: $\Delta Y\_A_{5\%} = 6.53 \pm 0.43\%$; 10% diameter changes: $\Delta Y\_A_{10\%} = 9.31 \pm 0.71\%$; 15% diameter changes: $\Delta Y\_A_{15\%} = 12.22 \pm 1.10\%$, N_arterioles = 35, mean (95% CI)), (h) The saturation changes ΔY maps of individual venules when the diameter of venules was assumed to be 50 μm and not to increase after sensory stimulation, (i) The saturation changes ΔY maps of individual arterioles when the diameter of arterioles was assumed to be 50 μm and dilate by 5% (the left panel), 10% (the middle panel) and 15% (the right panel) after sensory stimulation, (j) The mean saturation changes ΔY of venules and arterioles when the diameter of vessels was assumed to be 50 μm (ΔY_V = 6.36 ± 1.09%, N_venules = 25; 5% diameter changes: $\Delta Y\_A_{5\%} = 3.26 \pm 0.20\%$; 10% diameter changes: $\Delta Y\_A_{10\%} = 4.65 \pm 0.36\%$; 15% diameter changes: $\Delta Y\_A_{15\%} = 6.11 \pm 0.54\%$, N_arterioles = 35, mean (95% CI)).

In particular, in contrast to the ΔY calculated at 10% or 15% arteriole ΔV_f, the 5% arteriole ΔV_f provides more practical estimates of arteriole ΔY, which is also consistent with the previous optical ΔY measurements of arterioles with a diameter of 50 μm by Vazquez et al.[54]

It is important to note that the blood volume fraction (V_f) was estimated based on the actual mean size of the arteriole and venule ROIs identified in the A-V map. Since the arteriole voxels were determined based on the T1-weighted inflow effect and the venule voxels were mapped based on the T2* extravascular effects, the inherent MR contrast difference led to much larger blood volume estimates for venules than arterioles. Thus, when we estimated the blood volume fraction (V_f), we needed to consider the variability issue of V_f estimates, in particular for venule voxels given the large T2*-weighted extravascular effects. When we assigned

the different V_f values from venule voxels with varied sizes (top 20%: 50 μm, vs. the others: 35 μm), the baseline Y of 50 μm venules was 0.403 ± 0.098, which is slightly lower than that of the 35 μm venules (0.509 ± 0.088), and the ΔY of 50 μm venules was $11.4 \pm 2.67\%$, which is higher than that of the 35 μm venules $8.71 \pm 1.87\%$ (mean (95% CI), Supplementary Figure 7, Supplementary Table 2). The MESV-fMRI method provides an fMRI-based vessel-specific oxygen saturation level (Y) dynamic mapping scheme for the deep layer cortical penetrating vessels.

Discussion

The MESV-fMRI method offers two unique features when mapping the fMRI signal from individual vessels in the brain. The first is the short acquisition window (1–2 ms), which significantly shortens the minimal TE and excludes additional T_2* dephasing during echo acquisition. The other is the detection of the vessel-specific fMRI signal from multi-echoes with high spatiotemporal resolution. In this study, the fMRI signal was acquired at a sampling rate of 10 Hz over a field of view up to 9×6 mm of the rat cortex. Although only penetrating vessels (>30 μm) were identified by the A-V map,[76,77] the vessel-specific fMRI signal could be directly mapped in the deep layer cortex up to 1–1.5 mm, which is beyond the penetration depth of conventional optical methodology.[34] MESV-fMRI further extended the single-vessel mapping scheme to acquire the fMRI signal at different TEs, showing different T_1 or T_2* weighting, as well as the T2*-based fMRI signal. Although the line-scanning scheme with elongated total imaging time made it less practical for human brain mapping, the vessel-specific fMRI signal acquired at the deep layer cortex provided high-resolution experimental MRI data to potentially complement the vessel-specific quantitative modeling of the fMRI signal.[42,49,83–90]

The MESV-fMRI method allows differentiation of the intravascular and extravascular weighting from vessel and surrounding tissue voxels at different TEs. Consistent with previous experimental and model prediction studies,[42,91–93] the extravascular effect on venule voxels increased as a function of TE, which could be directly detected from peri-venule voxels (Figure 2(c)). Compared to the extravascular effect, the direct measurement of the intravascular effect was more challenging. The penetrating vessel size, characterized in the rat cortex by single-vessel fMRI or 2-PM imaging, ranges from 30 to 70 μm.[34,77] Despite the high spatial resolution, the fMRI signal from designated single-vessel voxels contained a good portion of partial volume effects from surrounding non-vessel parenchyma. Thus, the peak fMRI signal detected from the venule voxels remained partially extravascular-driven.[22] However, for very short TEs, the intravascular effect from the venule blood could not be neglected even at the high magnetic field (14.1 T). Though the fMRI signal detected at short TEs might not be as specific as in the spin-echo scheme, which excludes the extravascular effect by the refocusing pulse,[57,91,92,94] the intravascular effect contribution on the BOLD signal from venule voxels could be strong at the short TEs, in particular, at the 3 ms TE (Figure 2).

One novel application of MESV-fMRI is to detect fMRI signal changes from individual arterioles at different TEs. In contrast to the BOLD signal acquisition with EPI-fMRI, the direct CBV- and CBF-based signal was not detectable without a specific mapping sequence, e.g. arterial spin labeling[95,96] or vascular space occupancy,[97] or injection with a contrast agent for CBV.[5,98,99] The fMRI signal detected by MESV-fMRI at short TEs (e.g. 3 ms) is based on the T_1-weighted signal from voxels covering parenchyma enriched with capillaries or small arterioles with oxygenated blood. The vessel-specific inflow signal led to a significantly higher fMRI signal from the arteriole voxels compared to the peri-arteriole voxels (Figure 2(e)).[100] This could be directly due to the increased cerebral blood flow, given the arteriole dilation upon stimulation.[96] Interestingly, at long TEs, we did not observe the CBV-induced decrease of the fMRI signal either from the arteriole or peri-arteriole voxels from the averaged time courses as suggested for fMRI predictive models.[93] Using the pO_2-sensitive nanoprobe with 2-PM imaging, Gagnon et al.[42] detected oxygen levels of penetrating arterioles ranging from 70% to 95% at different vascular branches. As reported by Vazquez et al.,[54] the arterial oxygen saturation levels from 50 μm arterioles can be increased upon sensory stimulation and directly contribute to the increased BOLD signal, which can potentially cancel out the CBV-induced reduction of the TE-dependent signal. It is also interesting to note that the hyperbaric oxygen treatment to increase the pO_2 in the blood of the rat brain can potentially lead to T1 shortening,[101,102] which may contribute to the fMRI signal changes at shorter TEs in arterioles. Also, at longer TEs, the extravascular BOLD effect from venules could influence the signal changes at arteriole and peri-arteriole ROIs due to partial volume effects.

Similar to previous multi-echo EPI studies,[63,81,82] the T_2*-based functional map showed a much higher CNR than the T_2*-weighted functional maps acquired at each TE (Figure 3(d) and (e)). The temporal features of the vessel-specific hemodynamic signal can be better characterized to show an earlier onset time of the arteriole T_2*-based fMRI signal (0.92 ± 0.19 s) than that of the venule T_2*-based fMRI signal (1.14 ± 0.17 s).

The T_2*-based fMRI functional mapping represented a more significant vessel-specific onset time difference compared to previous single-vessel T_2*-weighted fMRI studies,[34] which could be due to the higher CNR of the T_2*-based fMRI signal. Also noteworthy is that the time-to-peak of the T_2*-based fMRI signal from arterioles was significantly shorter than that from the venules. The T_2*-based early arteriole fMRI signal onset and time-to-peak could result from the oxy/deoxy-hemoglobin ratio changes detected in arterioles,[38,54,103] as well as from the blood flow and volume contribution at short TEs (Supplementary Figure 6). The onset time of the fMRI signal detected by MESV-fMRI is similar to previous studies, indicating that the BOLD signal increased as early as 1 s after stimulus onset in both the cat and human visual cortex.[26,104] Meanwhile, Silva et al. used an M-sequence and showed faster BOLD-fMRI onset with a mean time-to-peak less than 2.5 s due to the short stimulation duration.[105] T_2*-based MESV-fMRI could better differentiate the temporal features of the fMRI signal from arteriole and venule voxels than the T_2*-weighted fMRI signal.[22,34]

MESV-fMRI-based T2* measurement from individual vessels penetrating the deep layer cortex demonstrates the possibility of directly modeling the hemodynamic signal contributing to the fMRI signal. We have performed the over-simplified estimation of the oxygenation saturation level (Y) and stimulation-induced changes (ΔY) from individual vessel voxels based on the assumed blood volume fraction (V_f) and its changes (ΔV_f) during stimulation using the analytical model developed by Yablonskiy and Haacke.[72] As shown in the Supplementary Tables 1 and 2, although the estimated Y and ΔY showed similar dynamic ranges as previously reported in the anesthetized rat[54,106] or mouse[107] brains, some large variations were detected when inappropriate V_f and ΔV_f values were used. For example, the baseline Y of venules with V_f at 0.15 (the diameter at 70 μm, Supplementary Table 1) was above 0.8, which is even higher than some smaller arteriole voxels.

Several key issues will need to be considered to better interpret the vessel-specific Y and ΔY estimation for future hemodynamic model validation. First, we performed a semi-quantitative estimation of the oxygen saturation (Y) based on the model of Yablonskiy and Haacke[72] for a single vessel of a voxel. In contrast to the advanced quantitative BOLD (qBOLD) modeling,[108–115] we oversimplified the resources of the magnetic inhomogeneity affecting the MR signal evolution for a given voxel. In particular, a more complicated model to incorporate the tissue and blood R2 contribution in combination with the macroscopic field inhomogeneity estimation[108,116] will be implemented for oxygen saturation estimation in our future studies. Second, we will need to develop a spin-echo based MESV-fMRI method to quantify the vessel-specific T2 values, which can provide a more accurate T2′ estimation than what has been applied in this work based on the previous measurement in rats using the same scanner.[73] Thirdly, previous qBOLD modeling has estimated the blood volume fraction (V_f) by either examining the dephasing effects of the deoxy-Hb of the venous blood (venous V_f),[109,117] or by applying the paramagnetic contrasts through the whole vessel network.[118–120] The MR-based V_f measurements have been less accurate than the optical imaging studies.[42,121] For MESV-fMRI, the estimation Y of the top 20% largest venules varied from 0.4 (the average diameter 50 μm, $V_f = 0.05$) to 0.69 (the average diameter 70 μm, $V_f = 0.098$) (Supplementary Figure 8). To improve the accuracy of the estimation of V_f of voxels for the major penetrating vessels, we will measure the vessel sizes with wide-field 2-PM imaging[40,122,123] followed by single-vessel fMRI mapping.[33] We can apply the single-vessel CBV-weighted fMRI measurement[33,34] to estimate the relative ΔV_f values for individual vessels with neuronal activation or by hypercapnia as a physiological reference for calibrated fMRI measurements from the same animals.[49] MESV-fMRI can also be potentially implemented in animal studies for nanosensor-based pO_2 measurement with 2-PM to validate the vessel-specific hemodynamic modeling to interpret the fMRI signal.[42] In addition, the model of Yablonskiy and Haacke[72] is based on the assumption of randomly oriented vessels. The significant impact of vessel orientations to gradient-echo fMRI has been reported by previous studies.[42,121] For a given penetrating vessel, the susceptibility effect of the vessel on the field inhomogeneity depends on the specific angle to the B_0 field. However, as shown in Figure 5, the estimated blood volume contribution to the vessel voxel ranges from 5 to 10%, which is only 2–2.5 times more than the averaged blood volume fraction (2–4%). There remains a large portion of the randomized microvascular contribution to the vessel voxels. For the future studies with the higher spatial resolution to increase the blood volume contribution from individual penetrating vessels to 25–50%, an orientation-specific delta R2* estimate should be assigned to different vessel voxels as suggested by previous studies.[42,121]

Finally, in contrast to EPI-fMRI with a conventional Cartesian or Spiral trajectory to cover the k-space, MESV-fMRI is less efficient and highly sensitive to motion artifacts. This is because the MESV-fMRI k-space was filled inconsecutively through the time series of the on/off block design. This line-scanning scheme leads to a great number of repetitions of the

block-design-based fMRI signal acquisition. Therefore, real-time signal acquisition in MESV-fMRI differed from multi-echo EPI-fMRI, and hence MESV-fMRI may not be used for non-BOLD component correction in the resting-state fMRI study.[124] This implies that the MESV-fMRI method would be less practical for human brain mapping and awake animal fMRI. However, this method can be readily used for ventilated and head-fixed animals under anesthesia. Using compressed sensing[125,126] and partial k-space imaging,[127,128] the acquisition time can be shortened significantly to enable implementation of MESV-fMRI in human brain mapping. In addition, MESV-fMRI was less sensitive to field inhomogeneity and fluctuation. It is less dependent on gradient performance and has shorter readout times than EPI-fMRI. These features allow MESV-fMRI to acquire images with a much higher spatiotemporal resolution than EPI-fMRI to directly decipher distinct vascular contributions to the fMRI signal with different hemodynamic features. The unique advantage of this method is the characterization of the vessel-specific neurovascular signaling events in the normal and diseased states, e.g. stroke or vascular/neuronal dementia, of animal models.

Contact for resource sharing

Any underlying research material related to the paper can be accessed from the corresponding author upon reasonable request.

Funding

The author(s) disclosed receipt of the following financial support for the research, authorship, and/or publication of this article: This research was supported by funding from the NIH Brain Initiative funding (RF1NS113278-01), the S10 instrument grant (S10 RR023009-01) to MGH/HST Martinos center, DFG YU 215/3-1, and internal funding from the Max Planck Society. YH acknowledges support from the European Union's Horizon 2020 research and innovation programme under the Marie Skłodowska-Curie Grant Agreement No. 843352, and the Lundbeck Foundation (R287-2018-479).

Acknowledgments

We would like to thank Dr. Pohmann R, Dr. Merkle H, and Buckenmaier K. for their technical support. We would like to thank Ms. Schulz H and Fischer S for their animal maintenance support. We would like to thank the AFNI team for their software support.

Declaration of conflicting interests

The author(s) declared no potential conflicts of interest with respect to the research, authorship, and/or publication of this article.

Authors' contributions

XY designed the research. YH, XY, MW performed the animal experiments; YH, XY acquired and analyzed the data; XY, YH wrote the paper.

ORCID iD

Yi He https://orcid.org/0000-0003-0040-9255

Supplementry material

Supplemental material for this article is available online.

References

1. Ogawa S, Tank DW, Menon R, et al. Intrinsic signal changes accompanying sensory stimulation: functional brain mapping with magnetic resonance imaging. *Proc Natl Acad Sci U S A* 1992; 89: 5951–5955.
2. Kwong KK, Belliveau JW, Chesler DA, et al. Dynamic magnetic resonance imaging of human brain activity during primary sensory stimulation. *Proc Natl Acad Sci U S A* 1992; 89: 5675–5679.
3. Kim SG and Ugurbil K. High-resolution functional magnetic resonance imaging of the animal brain. *Methods* 2003; 30: 28–41.
4. Ogawa S, Lee TM, Kay AR, et al. Brain magnetic resonance imaging with contrast dependent on blood oxygenation. *Proc Natl Acad Sci U S A* 1990; 87: 9868–9872.
5. Belliveau JW, Kennedy DN, Jr., McKinstry RC, et al. Functional mapping of the human visual cortex by magnetic resonance imaging. *Science* 1991; 254: 716–719.
6. Bandettini PA, Wong EC, Hinks RS, et al. Time course EPI of human brain function during task activation. *Magn Reson Med* 1992; 25: 390–397.
7. Turner R and Jones T. Techniques for imaging neuroscience. *Br Med Bull* 2003; 65: 3–20.
8. Turner R. Uses, misuses, new uses and fundamental limitations of magnetic resonance imaging in cognitive science. *Philos Transac R Soc B* 2016; 371: 20150349.
9. Goerke U, Garwood M and Ugurbil K. Functional magnetic resonance imaging using RASER. *Neuroimage* 2011; 54: 350–360.
10. Hu XP and Norris DG. Advances in high-field magnetic resonance imaging. *Annu Rev Biomed Eng* 2004; 6: 157–184.
11. Harel N, Bolan PJ, Turner R, Ugurbil K, Yacoub E. Recent advances in high-resolution MR application and its implications for neurovascular coupling research. *Front Neuroenerget* 2010; 2: 130.
12. Duyn JH. The future of ultra-high field MRI and fMRI for study of the human brain. *Neuroimage* 2012; 62: 1241–1248.

13. Yacoub E, Shmuel A, Pfeuffer J, et al. Imaging brain function in humans at 7 Tesla. *Magn Reson Med* 2001; 45: 588–594.
14. Menon RS, Ogawa S, Strupp JP, et al. Ocular dominance in human V1 demonstrated by functional magnetic resonance imaging. *J Neurophysiol* 1997; 77: 2780–2787.
15. Yacoub E, Harel N and Ugurbil K. High-field fMRI unveils orientation columns in humans. *Proc Nat Acad Sci U S A* 2008; 105: 10607–10612.
16. Kim DS, Duong TQ and Kim SG. High-resolution mapping of iso-orientation columns by fMRI. *Nat Neurosci* 2000; 3: 164–169.
17. Grinvald A, Slovin H and Vanzetta I. Non-invasive visualization of cortical columns by fMRI. *Nat Neurosci* 2000; 3: 105–107.
18. Cheng K, Waggoner RA and Tanaka K. Human ocular dominance columns as revealed by high-field functional magnetic resonance imaging. *Neuron* 2001; 32: 359–374.
19. Duong TQ, Kim DS, Ugurbil K, et al. Localized cerebral blood flow response at submillimeter columnar resolution. *Proc Nat Acad Sci U S A* 2001; 98: 10904–10909.
20. Fukuda M, Moon CH, Wang P, et al. Mapping iso-orientation columns by contrast agent-enhanced functional magnetic resonance imaging: reproducibility, specificity, and evaluation by optical imaging of intrinsic signal. *J Neurosci* 2006; 26: 11821–11832.
21. Heinzle J, Koopmans PJ, den Ouden HE, Raman S, Stephan KE. A hemodynamic model for layered BOLD signals. *Neuroimage* 2016; 125: 556–570.
22. Yu X, Glen D, Wang S, et al. Direct imaging of macrovascular and microvascular contributions to BOLD fMRI in layers IV–V of the rat whisker-barrel cortex. *Neuroimage* 2012; 59: 1451–1460.
23. Yu X, Qian C, Chen DY, et al. Deciphering laminar-specific neural inputs with line-scanning fMRI. *Nature Meth* 2014; 11: 55–58.
24. Polimeni JR, Fischl B, Greve DN, et al. Laminar analysis of 7T BOLD using an imposed spatial activation pattern in human V1. *Neuroimage* 2010; 52: 1334–1346.
25. Huber L, Goense J, Kennerley AJ, et al. Cortical lamina-dependent blood volume changes in human brain at 7 T. *Neuroimage* 2015; 107: 23–33.
26. Moon CH, Fukuda M and Kim SG. Spatiotemporal characteristics and vascular sources of neural-specific and -nonspecific fMRI signals at submillimeter columnar resolution. *Neuroimage* 2013; 64: 91–103.
27. Goense J, Merkle H and Logothetis NK. High-resolution fMRI reveals laminar differences in neurovascular coupling between positive and negative BOLD responses. *Neuron* 2012; 76: 629–639.
28. Shih YY, Chen YY, Lai HY, et al. Ultra high-resolution fMRI and electrophysiology of the rat primary somatosensory cortex. *Neuroimage* 2013; 73: 113–120.
29. Siero JC, Petridou N, Hoogduin H, et al. Cortical depth-dependent temporal dynamics of the BOLD response in the human brain. *J Cereb Blood Flow Metab* 2011; 31: 1999–2008.
30. Huber L, Handwerker DA, Jangraw DC, et al. High-resolution CBV-fMRI allows mapping of laminar activity and connectivity of cortical input and output in human M1. *Neuron* 2017; 96: 1253–1263.e7.
31. Kim SG, Jin T and Fukuda M. Spatial resolution of fMRI techniques. In: Ulmer S and Jansen O (eds) *fMRI: basics and clinical applications*. Springer: Berlin, Heidelberg, 2010, pp.15–21
32. Kim SG and Ogawa S. Biophysical and physiological origins of blood oxygenation level-dependent fMRI signals. *J Cereb Blood Flow Metab* 2012; 32: 1188–1206.
33. He Y, Wang M, Chen X, et al. Ultra-slow single-vessel BOLD and CBV-based fMRI spatiotemporal dynamics and their correlation with neuronal intracellular calcium signals. *Neuron* 2018; 97: 925–939.e5.
34. Yu X, He Y, Wang M, et al. Sensory and optogenetically driven single-vessel fMRI. *Nature Meth* 2016; 13: 337–340.
35. Silva AC and Koretsky AP. Laminar specificity of functional MRI onset times during somatosensory stimulation in rat. *Proc Natl Acad Sci U S A* 2002; 99: 15182–7.
36. Scheffler K and Lehnhardt S. Principles and applications of balanced SSFP techniques. *Eur Radiol* 2003; 13: 2409–18.
37. Scheffler K and Ehses P. High-resolution mapping of neuronal activation with balanced SSFP at 9.4 tesla. *Magn Reson Med* 2016; 76: 163–171.
38. Hillman EM, Devor A, Bouchard MB, et al. Depth-resolved optical imaging and microscopy of vascular compartment dynamics during somatosensory stimulation. *Neuroimage* 2007; 35: 89–104.
39. Devor A, Hillman EM, Tian P, et al. Stimulus-induced changes in blood flow and 2-deoxyglucose uptake dissociate in ipsilateral somatosensory cortex. *J Neurosci* 2008; 28: 14347–57.
40. Tian P, Teng IC, May LD, et al. Cortical depth-specific microvascular dilation underlies laminar differences in blood oxygenation level-dependent functional MRI signal. *Proc Natl Acad Sci U SA* 2010; 107: 15246–15251.
41. Shih AY, Driscoll JD, Drew PJ, et al. Two-photon microscopy as a tool to study blood flow and neurovascular coupling in the rodent brain. *J Cereb Blood Flow Metab* 2012; 32: 1277–1309.
42. Gagnon L, Sakadzic S, Lesage F, et al. Quantifying the microvascular origin of BOLD-fMRI from first principles with two-photon microscopy and an oxygen-sensitive nanoprobe. *J Neurosci* 2015; 35: 3663–3675.
43. Malonek D and Grinvald A. Interactions between electrical activity and cortical microcirculation revealed by imaging spectroscopy: implications for functional brain mapping. *Science* 1996; 272: 551–554.
44. Devor A, Dunn AK, Andermann ML, et al. Coupling of total hemoglobin concentration, oxygenation, and neural activity in rat somatosensory cortex. *Neuron* 2003; 39: 353–359.
45. Akons K, Dann EJ and Yelin D. Measuring blood oxygen saturation along a capillary vessel in human. *Biomed Opt Exp* 2017; 8: 5342–5348.

46. Tsytsarev V, Hu S, Yao J, et al. Photoacoustic microscopy of microvascular responses to cortical electrical stimulation. *J Biomed Opt* 2011; 16: 076002.
47. Uhlirova H, Kilic K, Tian P, et al. Cell type specificity of neurovascular coupling in cerebral cortex. *Elife* 2016; 5: pii: e14315.
48. Mishra A, O'Farrell FM, Reynell C, et al. Imaging pericytes and capillary diameter in brain slices and isolated retinae. *Nat Protoc* 2014; 9: 323–336.
49. Davis TL, Kwong KK, Weisskoff RM, et al. Calibrated functional MRI: mapping the dynamics of oxidative metabolism. *Proc Natl Acad Sci U SA* 1998; 95: 1834–1839.
50. Kennan RP, Scanley BE, Innis RB, et al. Physiological basis for BOLD MR signal changes due to neuronal stimulation: separation of blood volume and magnetic susceptibility effects. *Magn Reson Med* 1998; 40: 840–846.
51. Ogawa S, Menon RS, Tank DW, et al. Functional brain mapping by blood oxygenation level-dependent contrast magnetic resonance imaging. A comparison of signal characteristics with a biophysical model. *Biophys J* 1993; 64: 803–812.
52. Dickson JD, Ash TW, Williams GB, et al. Quantitative phenomenological model of the BOLD contrast mechanism. *J Magn Reson* 2011; 212: 17–25.
53. Huppert TJ, Allen MS, Diamond SG, et al. Estimating cerebral oxygen metabolism from fMRI with a dynamic multicompartment Windkessel model. *Hum Brain Mapp* 2009; 30: 1548–1567.
54. Vazquez AL, Fukuda M, Tasker ML, et al. Changes in cerebral arterial, tissue and venous oxygenation with evoked neural stimulation: implications for hemoglobin-based functional neuroimaging. *J Cereb Blood Flow Metab* 2010; 30: 428–439.
55. Kennerley AJ, Berwick J, Martindale J, et al. Concurrent fMRI and optical measures for the investigation of the hemodynamic response function. *Magn Reson Med* 2005; 54: 354–365.
56. Lee SP, Silva AC, Ugurbil K, et al. Diffusion-weighted spin-echo fMRI at 9.4 T: microvascular/tissue contribution to BOLD signal changes. *Magn Reson Med* 1999; 42: 919–928.
57. Duong TQ, Yacoub E, Adriany G, et al. Microvascular BOLD contribution at 4 and 7 T in the human brain: gradient-echo and spin-echo fMRI with suppression of blood effects. *Magn Reson Med* 2003; 49: 1019–1027.
58. Hyde JS, Biswal BB and Jesmanowicz A. High-resolution fMRI using multislice partial k-space GR-EPI with cubic voxels. *Magn Reson Med* 2001; 46: 114–125.
59. Goense JB and Logothetis NK. Laminar specificity in monkey V1 using high-resolution SE-fMRI. *Magn Reson Imag* 2006; 24: 381–392.
60. Budde J, Shajan G, Zaitsev M, et al. Functional MRI in human subjects with gradient-echo and spin-echo EPI at 9.4 T. *Magn Reson Med* 2014; 71: 209–218.
61. Yu X, Wang SM, Chen DY, et al. 3D mapping of somatotopic reorganization with small animal functional MRI. *Neuroimage* 2010; 49: 1667–1676.
62. Wang M, He Y, Sejnowski T, et al. Brain-state dependent astrocytic Ca2+ signals are coupled to both positive and negative BOLD-fMRI signals. *Proc Natl Acad Sci U SA* 2018; 115: E1647.
63. Chen NK and Wyrwicz AM. Correction for EPI distortions using multi-echo gradient-echo imaging. *Magn Reson Med* 1999; 41: 1206–1213.
64. Weiskopf N, Klose U, Birbaumer N, et al. Single-shot compensation of image distortions and BOLD contrast optimization using multi-echo EPI for real-time fMRI. *Neuroimage* 2005; 24: 1068–1079.
65. Poser BA, Versluis MJ, Hoogduin JM, et al. BOLD contrast sensitivity enhancement and artifact reduction with multiecho EPI: parallel-acquired inhomogeneity-desensitized fMRI. *Magn Reson Med* 2006; 55: 1227–1235.
66. Menon RS, Ogawa S, Tank DW, et al. Tesla gradient recalled echo characteristics of photic stimulation-induced signal changes in the human primary visual cortex. *Magn Reson Med* 1993; 30: 380–386.
67. Gonzales R, Woods R and Eddine S. *Digital image processing using MATLAB*. Knoxville, TN: Gatesmark Publishing, LLC, 2009.
68. Van Den Boomgaard R, Van Balen R. Methods for fast morphological image transforms using bitmapped binary images. *CVGIP: Graph Models Image Process* 1992; 54: 252–258.
69. Cox RW. AFNI: software for analysis and visualization of functional magnetic resonance neuroimages. *Comput Biomed Res* 1996; 29: 162–173.
70. Geissler A, Gartus A, Foki T, et al. Contrast-to-noise ratio (CNR) as a quality parameter in fMRI. *J Magn Reson Imaging* 2007; 25: 1263–1270.
71. Madsen MT. A simplified formulation of the gamma variate function. *Phys Med Biol* 1992; 37: 1597.
72. Yablonskiy DA and Haacke EM. Theory of NMR signal behavior in magnetically inhomogeneous tissues: the static dephasing regime. *Magn Reson Med* 1994; 32: 749–763.
73. Pohmann R, Shajan G and Balla D. Contrast at high field: relaxation times, magnetization transfer and phase in the rat brain at 16.4 T. *Magn Reson Med* 2011; 66: 1572–1581.
74. Kennan RP, Zhong J and Gore JC. Intravascular susceptibility contrast mechanisms in tissues. *Magn Reson Med* 1994; 31: 9–21.
75. Weisskoff RM and Kiihne S. MRI susceptometry: image-based measurement of absolute susceptibility of MR contrast agents and human blood. *Magn Reson Med* 1992; 24: 375–383.
76. Keller AL, Schuz A, Logothetis NK, et al. Vascularization of cytochrome oxidase-rich blobs in the primary visual cortex of squirrel and macaque monkeys. *J Neurosci* 2011; 31: 1246–1253.
77. Blinder P, Shih AY, Rafie C, et al. Topological basis for the robust distribution of blood to rodent neocortex. *Proc Natl Acad Sci U S A* 2010; 107: 12670–12675.
78. Blockley NP, Jiang L, Gardener AG, Ludman CN, Francis ST, Gowland PA. Field strength dependence

of R1 and R2* relaxivities of human whole blood to ProHance, Vasovist, and deoxyhemoglobin. *Magn Reson Med* 2008; 60: 1313–1320.
79. Jin T, Wang P, Tasker M, et al. Source of nonlinearity in echo-time-dependent BOLD fMRI. *Magn Reson Med* 2006; 55: 1281–1290.
80. Han S, Son JP, Cho H, et al. Gradient-echo and spin-echo blood oxygenation level-dependent functional MRI at ultrahigh fields of 9.4 and 15.2 Tesla. *Magn Reson Med* 2019; 81: 1237–1246.
81. Poser BA and Norris DG. Investigating the benefits of multi-echo EPI for fMRI at 7 T. *Neuroimage* 2009; 45: 1162–1172.
82. Kundu P, Brenowitz ND, Voon V, et al. Integrated strategy for improving functional connectivity mapping using multiecho fMRI. *Proc Natl Acad Sci U S A* 2013; 110: 16187–16192.
83. Leontiev O, Dubowitz DJ and Buxton RB. CBF/CMRO2 coupling measured with calibrated BOLD fMRI: sources of bias. *Neuroimage* 2007; 36: 1110–1122.
84. Boxerman JL, Bandettini PA, Kwong KK, et al. The intravascular contribution to fMRI signal change: Monte Carlo modeling and diffusion-weighted studies in vivo. *Magn Reson Med* 1995; 34: 4–10.
85. Gagnon L, Smith AF, Boas DA, et al. Modeling of cerebral oxygen transport based on in vivo microscopic imaging of microvascular network structure, blood flow, and oxygenation. *Front Comput Neurosci* 2016; 10: 82.
86. Buxton RB. Dynamic models of BOLD contrast. *Neuroimage* 2012; 62: 953–961.
87. Buxton RB, Wong EC and Frank LR. Dynamics of blood flow and oxygenation changes during brain activation: the balloon model. *Magn Reson Med* 1998; 39: 855–864.
88. Buxton RB, Uludağ K, Dubowitz DJ, et al. Modeling the hemodynamic response to brain activation. *Neuroimage* 2004; 23: S220–S233.
89. Griffeth VE and Buxton RB. A theoretical framework for estimating cerebral oxygen metabolism changes using the calibrated-BOLD method: modeling the effects of blood volume distribution, hematocrit, oxygen extraction fraction, and tissue signal properties on the BOLD signal. *Neuroimage* 2011; 58: 198–212.
90. Buxton RB and Frank LR. A model for the coupling between cerebral blood flow and oxygen metabolism during neural stimulation. *J Cereb Blood Flow Metab* 1997; 17: 64–72.
91. Yacoub E, Duong TQ, Van De Moortele PF, et al. Spin-echo fMRI in humans using high spatial resolutions and high magnetic fields. *Magn Reson Med* 2003; 49: 655–664.
92. Jochimsen TH, Norris DG, Mildner T, et al. Quantifying the intra- and extravascular contributions to spin-echo fMRI at 3 T. *Magn Reson Med* 2004; 52: 724–732.
93. Uludag K, Muller-Bierl B and Ugurbil K. An integrative model for neuronal activity-induced signal changes for gradient and spin echo functional imaging. *Neuroimage* 2009; 48: 150–165.
94. Ugurbil K, Toth L and Kim DS. How accurate is magnetic resonance imaging of brain function? *Trends Neurosci* 2003; 26: 108–114.
95. Detre JA, Leigh JS, Williams DS, et al. Perfusion imaging. *Magn Reson Med* 1992; 23: 37–45.
96. Kim T, Hendrich KS, Masamoto K, et al. Arterial versus total blood volume changes during neural activity-induced cerebral blood flow change: implication for BOLD fMRI. *J Cereb Blood Flow Metab* 2007; 27: 1235–1247.
97. Lu H, Golay X, Pekar JJ, et al. Functional magnetic resonance imaging based on changes in vascular space occupancy. *Magn Reson Med* 2003; 50: 263–274.
98. Lee SP, Duong TQ, Yang G, et al. Relative changes of cerebral arterial and venous blood volumes during increased cerebral blood flow: implications for BOLD fMRI. *Magn Reson Med* 2001; 45: 791–800.
99. Kim T and Kim SG. Temporal dynamics and spatial specificity of arterial and venous blood volume changes during visual stimulation: implication for BOLD quantification. *J Cereb Blood Flow Metab* 2011; 31: 1211–1222.
100. Kim SG, Hendrich K, Hu X, et al. Potential pitfalls of functional MRI using conventional gradient-recalled echo techniques. *NMR Biomed* 1994; 7: 69–74.
101. Muir ER, Cardenas DP and Duong TQJN. MRI of brain tissue oxygen tension under hyperbaric conditions. *Neuroimage* 2016; 133: 498–503.
102. Uematsu H, Takahashi M, Hatabu H, et al. Changes in T1 and T2 observed in brain magnetic resonance imaging with delivery of high concentrations of oxygen. *J Comput Assist Tomograph* 2007; 31: 662–665.
103. Berwick J, Johnston D, Jones M, et al. Neurovascular coupling investigated with two-dimensional optical imaging spectroscopy in rat whisker barrel cortex. *Eur J Neurosci* 2005; 22: 1655–1666.
104. Lin FH, Witzel T, Raij T, et al. fMRI hemodynamics accurately reflects neuronal timing in the human brain measured by MEG. *Neuroimage* 2013; 78: 372–384.
105. Silva AC, Koretsky AP and Duyn JH. Functional MRI impulse response for BOLD and CBV contrast in rat somatosensory cortex. *Magn Reson Med* 2007; 57: 1110–1118.
106. Vazquez AL, Fukuda M and Kim SG. Evolution of the dynamic changes in functional cerebral oxidative metabolism from tissue mitochondria to blood oxygen. *J Cereb Blood Flow Metab* 2012; 32: 745–758.
107. Sakadzic S, Mandeville ET, Gagnon L, et al. Large arteriolar component of oxygen delivery implies a safe margin of oxygen supply to cerebral tissue. *Nat Commun* 2014; 5: 5734.
108. Christen T, Lemasson B, Pannetier N, et al. Evaluation of a quantitative blood oxygenation level-dependent (qBOLD) approach to map local blood oxygen saturation. *NMR Biomed* 2011; 24: 393–403.
109. He X and Yablonskiy DA. Quantitative BOLD: mapping of human cerebral deoxygenated blood volume and oxygen extraction fraction: default state. *Magn Reson Med* 2007; 57: 115–126.

110. Lee H, Englund EK and Wehrli FW. Interleaved quantitative BOLD: combining extravascular R2′-and intravascular R2-measurements for estimation of deoxygenated blood volume and hemoglobin oxygen saturation. *Neuroimage* 2018; 174: 420–431.
111. An H and Lin W. Quantitative measurements of cerebral blood oxygen saturation using magnetic resonance imaging. *J Cereb Blood Flow Metab* 2000; 20: 1225–1236.
112. He X, Zhu M and Yablonskiy DA. Validation of oxygen extraction fraction measurement by qBOLD technique. *Magn Reson Med* 2008; 60: 882–888.
113. Fujita N, Shinohara M, Tanaka H, et al. Quantitative mapping of cerebral deoxyhemoglobin content using MR imaging. *Neuroimage* 2003; 20: 2071–2083.
114. Stone AJ and Blockley NP. A streamlined acquisition for mapping baseline brain oxygenation using quantitative BOLD. *Neuroimage* 2017; 147: 79–88.
115. Stone AJ, Holland NC, Berman AL, et al. Simulations of the effect of diffusion on asymmetric spin echo based quantitative BOLD: an investigation of the origin of deoxygenated blood volume overestimation. *Neuroimage* 2019; 201: 116035.
116. Yang QX, Williams GD, Demeure RJ, et al. Removal of local field gradient artifacts in T2*-weighted images at high fields by gradient-echo slice excitation profile imaging. *Magn Reson Med* 1998; 39: 402–409.
117. DeFelipe J, Alonso-Nanclares L and Arellano JI. Microstructure of the neocortex: comparative aspects. *J Neurocytol* 2002; 31: 299–316.
118. Tropres I, Lamalle L, Peoc'h M, et al. In vivo assessment of tumoral angiogenesis. *Magn Reson Med* 2004; 51: 533–541.
119. Zaharchuk G. Theoretical basis of hemodynamic MR imaging techniques to measure cerebral blood volume, cerebral blood flow, and permeability. *Am J Neuroradiol* 2007; 28: 1850–1858.
120. Tropres I, Grimault S, Vaeth A, et al. Vessel size imaging. *Magn Reson Med* 2001; 45: 397–408.
121. Báez-Yánez MG, Ehses P, Mirkes C, et al. The impact of vessel size, orientation and intravascular contribution on the neurovascular fingerprint of BOLD bSSFP fMRI. *Neuroimage* 2017; 163: 13–23.
122. Nishimura N, Schaffer CB, Friedman B, et al. Penetrating arterioles are a bottleneck in the perfusion of neocortex. *Proc Natl Acad Sci U S A* 2007; 104: 365–370.
123. Mateo C, Knutsen PM, Tsai PS, et al. Entrainment of arteriole vasomotor fluctuations by neural activity is a basis of blood-oxygenation-level-dependent "resting-state" connectivity. *Neuron* 2017; 96: 936–948.
124. Kundu P, Inati SJ, Evans JW, et al. Differentiating BOLD and non-BOLD signals in fMRI time series using multi-echo EPI. *Neuroimage* 2012; 60: 1759–1770.
125. Lustig M, Donoho D and Pauly JM. Sparse MRI: the application of compressed sensing for rapid MR imaging. *Magn Reson Med* 2007; 58: 1182–1195.
126. Lustig M, Donoho DL, Santos JM, et al. Compressed sensing MRI. *IEEE Signal Process Mag* 2008; 25: 72.
127. Hyde JS, Biswal BB and Jesmanowicz A. High-resolution fMRI using multislice partial k-space GR-EPI with cubic voxels. *Magn Reson Med* 2001; 46: 114–125.
128. Jesmanowicz A, Bandettini PA and Hyde JS. Single-shot half k-space high-resolution gradient-recalled EPI for fMRI at 3 Tesla. *Magn Reson Med* 1998; 40: 754–762.